Characterization of aerosol particles at Cape Verde close to sea and cloud level heights - Part 1: particle number size distribution, cloud condensation nuclei and their origins

Xianda Gong[1], Heike Wex[1], Jens Voigtländer[1], Khanneh Wadinga Fomba[1], Kay Weinhold[1], Manuela van Pinxteren[1], Silvia Henning[1], Thomas Müller[1], Hartmut Herrmann[1], and Frank Stratmann[1]

[1]Leibniz Institute for Tropospheric Research, Leipzig, Germany

Correspondence: Xianda Gong (gong@tropos.de)

S1   Accounting for particle losses

The particle losses related to the transport of aerosol particles within the inlet tube system are determined using the Particle Loss Calculator (PLC) (von der Weiden et al., 2009). Size-dependent particle losses due to diffusion, sedimentation, turbulent inertial deposition, inertial deposition in a bend, and inertial deposition in a contraction are accounted for. The resulting particle losses is shown in Fig. S1, which depicts particle loesses in % as a function of particle size.
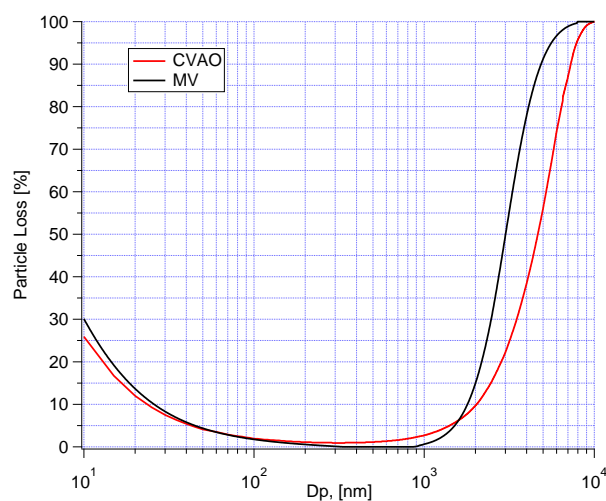
Figure S1. Size-dependent particle loss through the inlet at at the site close to sea level (CVAO) and on the mountaintop (MV).

S2 Monte Carlo simulation

The uncertainty in κ, which results from uncertainties of the PNSD measurements and the supersaturations of the CCNc, was determined by applying a Monte Carlo simulation (MCS) in a similar fashion as done by Kristensen et al. (2016) and Herenz et al. (2018).

The particle diameter which is selected with a differential mobility analyzer (DMA) has an uncertainty of 3.0% (corresponding to one standard deviation). The measured particle number concentration has an uncertainty of 5.0% (corresponding to one standard deviation). In addition, the effective supersaturation in CCNc has a relative uncertainty of 3.5% (corresponding to one standard deviation) for supersaturation above 0.20%. Below a supersaturation of 0.20%, the same absolute uncertainty as for a supersaturation of 0.20% can be assumed. These uncertainties have been inferred from several supersaturation calibrations that were performed at the Leibniz Institute for Tropospheric Research (TROPOS). All of the measurement uncertainties can be found in the ACTRIS protocol (Gysel and Stratmann, 2013). To consider the impact of these uncertainties on d_{crit} and κ in a realistic way, a Monte Carlo simulation (MCS) based on random normal distributions was used. This following general equation was applied:

$$s_{\mathrm{MC}} = s + s * u * p \tag{S1}$$

where u is the relative uncertainty, p is a random number, s is the measured signal and s_{MC} is the resulting MCS signal. This was done for 10 000 random and normally distributed numbers p, with a mean of 0 and a standard deviation of 1, which then results in 10 000 values for s_{MC} with a variability that is characterized by u.

Firstly, the uncertainty in d_{crit} was obtained by a MCS based on one exemplary PNSDs, the related N_{CCN} and a 5.0% uncertainty in the particle number concentration. Eq. S1 was used to vary the particle number concentration of each size bin of the PNSD to calculate 10 000 d_{crit} values, of which a distribution is shown in Fig. S2(a). The mean and 1 standard deviation of these 10 000 d_{crit} values can be taken from this distribution, and the overall uncertainty in d_{crit} was derived from those values together with the 3.0% uncertainty in the particle sizing due to the DMA, using error propagation. This was then done for all PNSDs. The resulting uncertainties are shown as error bars in the middle panel of Fig. 10.

Secondly, κ and the corresponding error bars in the lower panel of Fig. 10 are inferred by means of Eq. 1. The effective supersaturation of the CCNc are 10 000 times Monte Carlo simulated (same procedure as for d_{crit}). Since the connection between κ and supersaturation is logarithmic, the resulting distribution of the 10 000 κ values is a log-normal distribution, as can be seen in Fig. S2(b) for one exemplary case. Consequently, our final inferred κ and its uncertainty are the geometric mean and the one standard geometric standard deviation of this distribution, respectively. The resulting uncertainties are shown as error bars in the lower panel of Fig. 10.

Lastly, we calculated d_{crit} and κ uncertainties in a certain period. Combining all d_{crit} values in a certain period, we could get the total d_{crit} distribution. In this case, we took all of the d_{crit} at a supersaturation of 0.50% during the whole campaign and the resulting distribution are shown in Fig. S2(c). The mean value and one standard deviation of d_{crit} can be taken from this distribution, which is shown in Fig. 11(d) and Fig. 12(b). Using the same way, we did the same distribution of κ values.
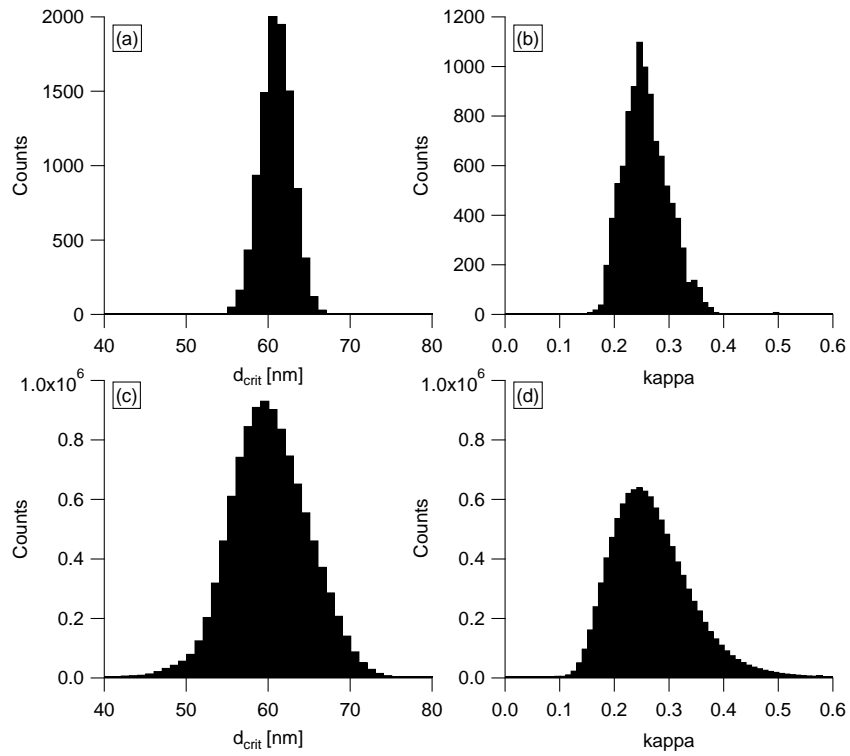
Figure S2. (a) Distribution of 10 000 d_{crit} values after applying the MCS. (b) Distribution of 10 000 κ values after applying the MCS. (c) Distribution of d_{crit} values over a certain period. (d) Distribution of κ values over a certain period.

The geometric mean value and one geometric standard deviation of κ can be taken from this distribution, which is shown in Fig. 11(d) and Fig. 12(b).

S3   Balloon measurement

Balloon measurements were carried out at CVAO. One example of the result from such a measurement at 14:30 UTC on 17 September is shown in Fig. S3, including vertical profile of temperature and relative humility. The weather condition at that moment is shown in Fig. S4.
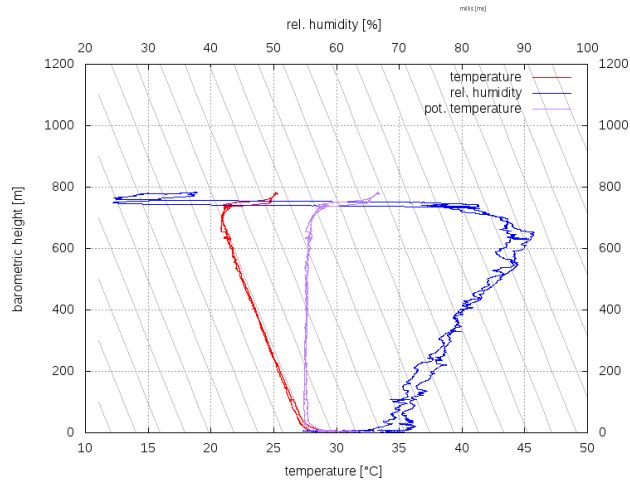

Figure S3. Vertical profile of temperature and relative humidity at 14:30 UTC on 17 September. Profiles up to about 1200 m can be measured. From the measurements the inversion layer height was determined (here: ∼700 m).

Figure S4. Picture of weather condition at 14:30 UTC on 17 September.

S4   Particle classification

Fig. S5 shows the probability density function (PDF) of N_{coarse}. Two distinct modes of PDF were observed, i.e., small mode in the range from 0 to 25 cm^{-3}, large mode in the range large than 25 cm^{-3}. Based on a ground measurement at CVAO, Schladitz et al. (2011) found the particle number concentration of the coarse mode (N_{coarse}) is highly variable and the higher N_{coarse} originates from the Saharan desert. We assumed that $N_{coarse} > 25$ cm^{-3} is mainly contributed by dust aerosols.
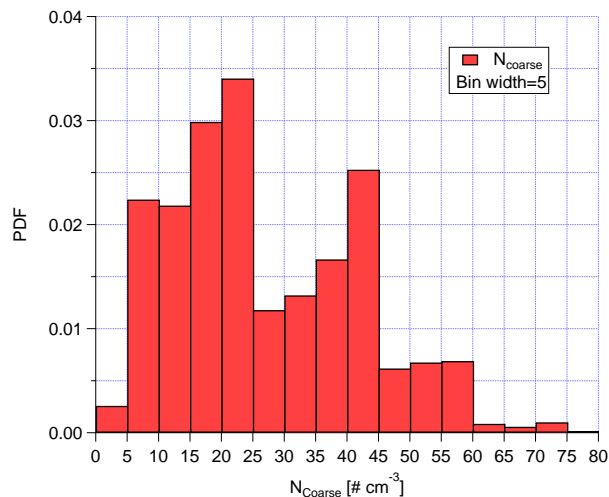
Figure S5. PDF of N_{coarse} during the whole campaign.

## S5 Correlation of N_{coarse} with wind speed during marine period

Fig. S6 shows N_{coarse} as a function of wind speed during the marine type period. The coefficient of determination (R^2) is 0.69 and p value is <0.01, which means a good correlation between coarse mode number concentration and wind speed. This is consistent with the fact that these particles come from sea spray, i.e., are SSA (sea spray aerosol), generated from the process

5 associated with the agitation of the sea surface by air moving above it.
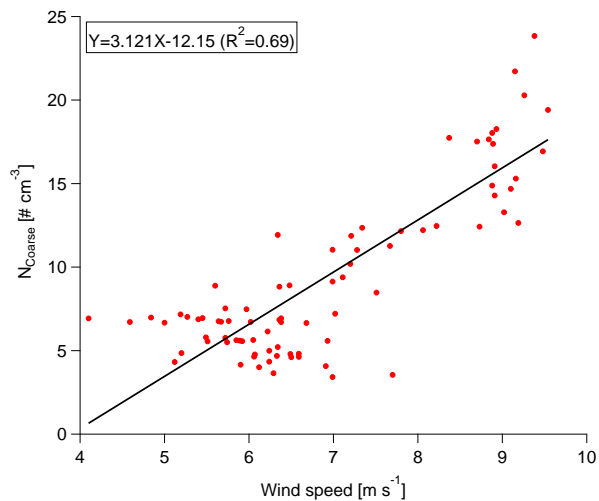
Figure S6. N_{coarse} as a function of wind speed during the marine type period. The liner fitting function and R^2 are given in the panel.

S6 Characterization of cloud events

Fig. S7 shows PDF of the ratio of $N^{\mathrm{MV}}_{\mathrm{accumulation}}$ to $N^{\mathrm{CVAO}}_{\mathrm{accumulation}}$ in the upper panel. Clearly, three modes were observed. The largest mode is located at the ratio of 1. The minimum between largest mode and smaller modes is at 0.85. Therefore, 0.85 can be used as a threshold to classify cloud events and non-cloud events. For the periods when the three-modal log-normal fitting

5   function did not work (from 03:30 to 20:00 21 and 09:30 28 to 18:30 30 September), we used the ratio of $N^{\mathrm{MV}}_{\mathrm{80\text{-}800nm}}$ to $N^{\mathrm{CVAO}}_{\mathrm{80\text{-}800nm}}$ and the PDF of this ratio can be seen in the lower panel in Fig. S7. When the ratio is lower than 0.75, we assume that MV is in a cloud. These two ratios were derived separately for different cases with three- and bi-modal fitting and they are different.
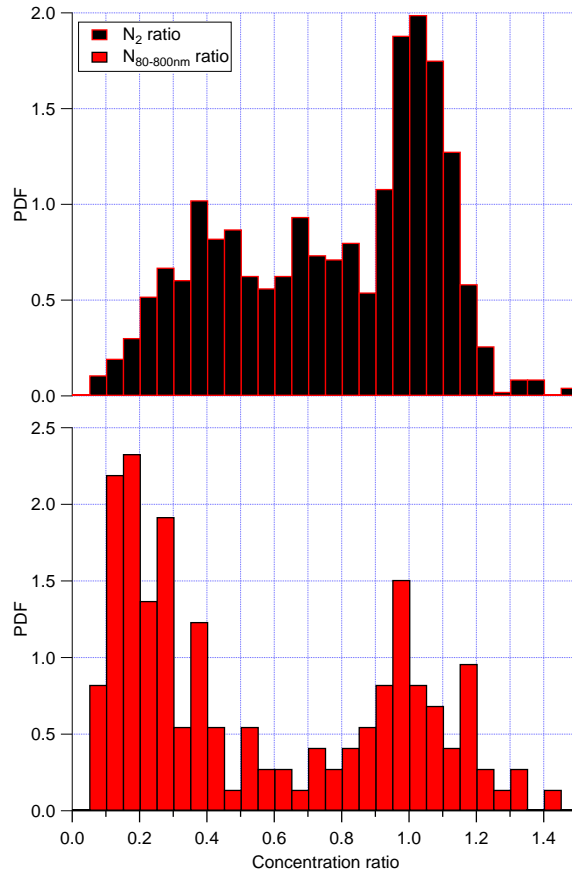
Figure S7. PDF of the ratio between $N^{\mathrm{MV}}_{\mathrm{accumulation}}$ and $N^{\mathrm{CVAO}}_{\mathrm{accumulation}}$ in the upper panel and the ratio between $N^{\mathrm{MV}}_{\mathrm{80\text{-}800nm}}$ and $N^{\mathrm{CVAO}}_{\mathrm{80\text{-}800nm}}$ in the lower panel.

The resulting times for the occurrence of cloud events is shown by red shadows in Fig. S8. Time series of RH at MV is shown by a black line in Fig. S8. It is clear that times with RH=100% are consistent with cloud events identified as described above, which verifies our identification of cloud events.
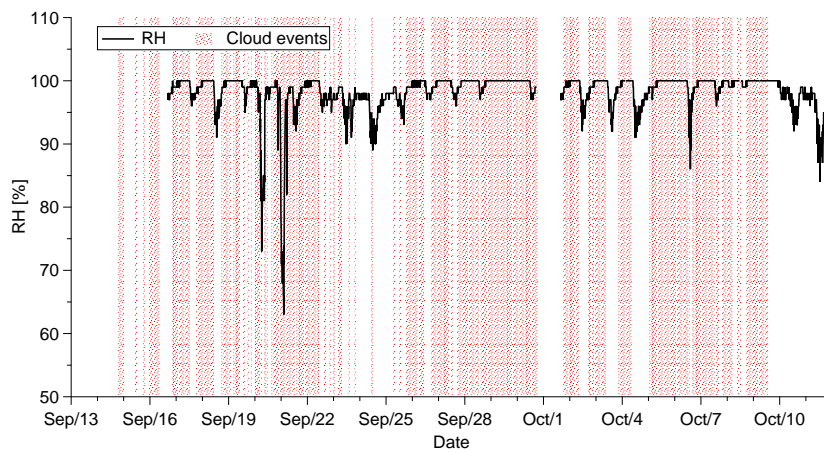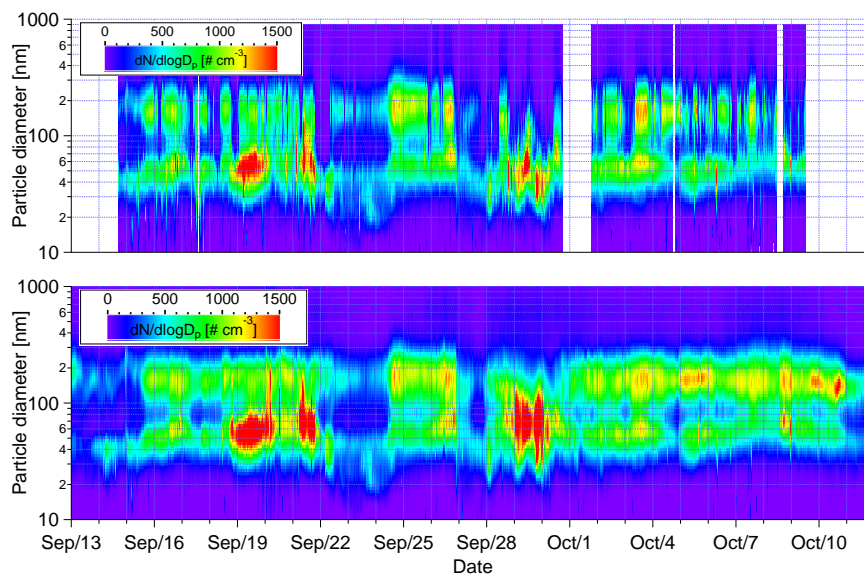

Figure S8. Time series of RH at MV is shown by black line. Cloud event times are shown by red shadows.

## S7   Contour plots for PNSDs at CVAO and MV

Fig. S9 shows the contour plots for PNSDs in the size range between 10 to 800 nm at MV in the upper panel and at CVAO in the lower panel.

Figure S9. Contour plots for PNSDs in the size range between 10 to 800 nm at MV (upper panel) and at CVAO (lower panel). The color scale indicates dN/dlogDp in cm^{-3}.

S8 PNSDs at MV and CVAO during decoupled boundary layer period

Fig. S10 shows PNSDs at MV (red lines) and CVAO (black lines) from 10:30 to 11:00 16 September. This was a period during which a decoupled boundary layer was observed, and even in this case, PNSDs were similar at MV and CVAO.
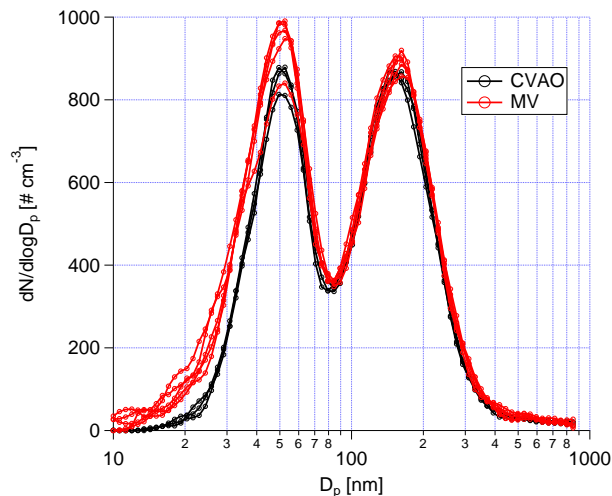
Figure S10. PNSDs at MV (in red) and CVAO (in black) from 10:30 to 11:00 16 September.

S9 Explanation of larger error bars for d_{crit} and κ at 0.30% during marine periods

At a supersaturation of 0.30% during the marine periods, κ and d_{crit} featured the largest observed variability. This can be seen from the larger error bars in Fig. 12. d_{crit} at 0.30% is close to the Hoppel minimum, and the particle number concentration (dN/dlogDp) around the Hoppel minimum is lower than 100 cm^{-3}. Assuming N_{CCN} varied 2% during each ~6-minute averaged period, the absolute number concentration can change around 5 cm^{-3}. The tiny variation of N_{CCN} can change d_{crit} by ~10 nm. Since κ is correlated to d_{crit}^3, the large error bar of κ results. To conclude, these larger error bars at a supersaturation of 0.30% are due to the measurement uncertainty.

10

References

Gysel, M. and Stratmann, F.: WP3 - NA3: In-situ chemical, physical and optical properties of aerosols, Deliverable D3.11: Standardized protocol for CCN measurements, Tech. rep., http://www.actris.net/Publications/ACTRISQualityStandards/tabid/11271/language/en-GB/Default.aspx, 2013.

5 Herenz, P., Wex, H., Henning, S., Kristensen, T. B., Rubach, F., Roth, A., Borrmann, S., Bozem, H., Schulz, H., and Stratmann, F.: Measurements of aerosol and CCN properties in the Mackenzie River delta (Canadian Arctic) during spring–summer transition in May 2014, Atmos. Chem. Phys., 18, 4477–4496, https://doi.org/10.5194/acp-18-4477-2018, https://www.atmos-chem-phys.net/18/4477/2018/, 2018.

Kristensen, T. B., Müller, T., Kandler, K., Benker, N., Hartmann, M., Prospero, J. M., Wiedensohler, A., and Stratmann, F.: Properties of cloud condensation nuclei (CCN) in the trade wind marine boundary layer of the western North Atlantic, Atmos. Chem. Phys., 16, 2675–2688,

10 https://doi.org/10.5194/acp-16-2675-2016, http://www.atmos-chem-phys.net/16/2675/2016/, 2016.

Schladitz, A., Müller, T., Nowak, A., Kandler, K., Lieke, K., Massling, A., and Wiedensohler, A.: In situ aerosol characterization at Cape Verde, Part1: Particle number size distributions, hygroscopic growth and state of mixing of mrine and Saharan dust aerosol, Tellus B, 63, 531–548, https://doi.org/10.1111/j.1600-0889.2011.00569.x, http://dx.doi.org/10.1111/j.1600-0889.2011.00569.x, 2011.

von der Weiden, S. L., Drewnick, F., and Borrmann, S.: Particle Loss Calculator - a new software tool for the assessment of the performance

15 of aerosol inlet systems, Atmos. Meas. Tech., 2, 479–494, https://doi.org/10.5194/amt-2-479-2009, http://www.atmos-meas-tech.net/2/479/2009/, 2009.